Dalton Transactions

ROYAL SOCIETY OF CHEMISTRY

PAPER

View Article Online
View Journal | View Issue

Cite this: *Dalton Trans.*, 2026, **55**, 2471

Optimal Mn doping for enhanced photothermal conversion performance in Prussian blue@layered double hydroxides

Weixin Mo, [a] Liming Yang,[b] Xinggui Gu, [b] Huiyu Li[a] and Yongjun Feng *[a]

Received 19th November 2025,
Accepted 5th January 2026

DOI: 10.1039/d5dt02778k

rsc.li/dalton

Near-infrared (NIR)-responsive photothermal materials are critical for solar energy conversion, yet conventional materials face limitations in efficiency, stability, and spectral tunability. Herein, we report Mn-doped Prussian blue intercalated MgAl-layered double hydroxides (Mn-PB@LDHs), synthesized *via* a separate nucleation and aging steps (SNAS) method, which exhibit synergistic enhancement in photothermal performance and stability. The optimized Mn-PB@LDH-3 exhibits a high photothermal conversion efficiency (75.10% under 808 nm laser light, 0.5 W cm^{-2}) and solar-driven water evaporation performance (1.60 kg m^{-2} h^{-1}, 97.93% under 1 kW m^{-2} simulated sunlight). Moderate Mn^{2+} doping optimizes Prussian blue's electronic structure by enhancing metal-to-metal charge transfer and reducing resistance, while an excessive doping amount induces Jahn–Teller distortion and electron localization, impairing efficiency. The MgAl-LDH host confers stability *via* nanoconfinement (suppressing structural degradation) and electrostatic interactions (inhibiting metal leaching under alkaline conditions). This work presents a high-performance, stable photothermal material and establishes a generalizable host–guest strategy for advanced solar energy conversion applications.

Introduction

Near-infrared (NIR) light has garnered substantial research interest due to its uniquely advantageous properties, including relatively high photon energy, low tissue absorption and scattering, deep tissue penetration, and dark-field imaging capability.[1,2] These inherent attributes have further stimulated considerable exploration across a wide range of applications, such as photothermal and photoacoustic (PT/PA) imaging,[3,4] NIR laser-assisted photothermal therapy (PTT),[5] night-vision sensors,[6] and photothermal-electric devices.[7] At the core of these applications lies the photothermal conversion process, which typically proceeds through non-radiative relaxation or localized surface plasmon resonance (LSPR) pathways.[8] Nevertheless, despite these favorable characteristics, conventional NIR-absorbing molecular systems—often relying on a single photothermal conversion route—are often plagued by complex synthetic procedures, poor photostability, and high production costs. Thus, robust and highly stable photothermal materials with multiple energy conversion pathways are highly desirable.

Prussian blue (PB) is a classical coordination nanomaterial with a face-centered cubic structure (space group *Fm*3*m*). Composed of ferric (Fe^{3+}), ferrous (Fe^{2+}), and cyanide (CN^{-}) ions, it has emerged as a versatile functional material with growing technological relevance.[9,10] Its intrinsic magnetism, tunable electrochemical activity, and excellent biocompatibility have driven significant research interest, enabling applications in electrochemical sensing,[11] batteries,[12] energy storage devices,[13] and magnetic resonance imaging (MRI).[14] Beyond these domains, PB nanoparticles have also demonstrated considerable promise for photothermal and photoacoustic (PT/PA) imaging[15] due to their strong near-infrared (NIR) absorption and efficient photothermal conversion *via* both non-radiative relaxation and localized surface plasmon resonance (LSPR) effects.[16] Nevertheless, two key limitations constrain their photothermal performance: (i) the intrinsic absorption peak, which frequently mismatches the emission spectra of commercial NIR lasers, leading to reduced light-to-heat conversion efficiency;[14,16] and (ii) a strong tendency toward aggregation in aqueous media, which significantly deteriorates photothermal output.[17] To mitigate these challenges, compositional modification strategies such as heteroatom doping[18] and structural engineering to suppress aggregation have been actively explored as critical pathways. Among these, Mn doping to tune the photothermal conversion performance of the Prussian blue component, allowing precise regulation of its properties, has been revealed to be an efficient pathway.[14,19]

[a]*State Key Laboratory of Chemical Resource Engineering, College of Chemistry, Beijing University of Chemical Technology, Beijing, 100029, China. E-mail: yjfeng@mail.buct.edu.cn*

[b]*Beijing Advanced Innovation Center for Soft Matter Science and Engineering, State Key Laboratory of Chemical Resource Engineering, College of Materials Science and Engineering, Beijing University of Chemical Technology, Beijing, 100029 China*

Layered double hydroxides (LDHs) are a family of anionic clays featuring positively charged brucite-like layers stabilized by interlayer anions and water molecules, representing a versatile class of functional materials with tunable structural and chemical properties.[20] Their general chemical formula, $[M^{2+}_{1-x}M^{3+}_{x}(OH)_2]^{x+}A^{n-}_{x/n}{\cdot}yH_2O$ (where M^{2+} and M^{3+} denote divalent and trivalent metal cations, respectively, and A^{n-} represents compensating interlayer anions),[21,22] underscores their inherent compositional flexibility. Owing to their structural adaptability, excellent synthesis controllability and robust stability, LDHs have been widely utilized in diverse technological fields, including catalysis,[23] adsorption,[24] and drug delivery systems.[25] Beyond these conventional applications, the layered architecture of LDHs confers unique advantages for photothermal enhancement. The nanoscale confinement effects and electrostatic host–guest interactions can stabilize intercalated functional species, suppress aggregation, and thereby markedly enhance the photothermal conversion efficiency of embedded light-absorbing materials. However, different synthesis methods affect the properties of LDHs. Among these, a separate nucleation and aging (SNA) method enables controllable intercalation and structural optimization of LDHs, thereby enhancing interlayer anion diffusion between layers. Moreover, LDH nanosheets prepared *via* the SNA method exhibit improved dispersion uniformity, which reduces aggregation of LDH crystals and promotes subsequent introduction of metal ions.[26,27]

Combining the advantages of both PB and LDHs, we herein engineer a high-efficiency photothermal conversion system through the intercalation of PB into MgAl-LDH layers *via* a separate nucleation and aging (SNA) method, complemented by controlled Mn^{2+} doping to optimize optical responses, *cf*, Scheme 1. This work not only establishes a synergistic strategy combining Mn^{2+} doping and LDH nanoscale confinement to advance PB-based photothermal materials but also provides fundamental insights for the rational design of advanced inorganic composites in next-generation photothermal applications.

Experimental section

Chemicals

All chemicals were used as received without further purification. Potassium ferricyanide ($K_3[Fe(CN)_6]$), sodium hydroxide (NaOH), and aluminum nitrate nonahydrate ($Al(NO_3)_3{\cdot}9H_2O$) were purchased from Aladdin (Shanghai, China). Magnesium nitrate hexahydrate ($Mg(NO_3)_2{\cdot}6H_2O$) and ferrous chloride tetrahydrate ($FeCl_2{\cdot}4H_2O$) were supplied by Sinopharm Chemical Reagent Co., Ltd. Manganese chloride ($MnCl_2$) was obtained from Macklin (Shanghai, China).

Synthesis of PF-LDHs and Mn-doped PB@LDHs

Synthesis of PF-LDHs. The ferricyanide-intercalated MgAl-LDHs (labeled as PF-LDHs) were synthesized *via* the previously established separate nucleation and aging steps (SNAS) method.[26] Briefly, a salt solution (solution A) was first prepared by dissolving 16.4102 g (64 mmol) of $Mg(NO_3)_2{\cdot}6H_2O$ and 12.0042 g (32 mmol) of $Al(NO_3)_3{\cdot}9H_2O$ in 400 mL of deionized water. Concurrently, an alkaline precursor solution (solution B) was formulated by dissolving 7.6800 g (0.192 mol) of NaOH and 6.9142 g (21 mmol) of $K_3[Fe(CN)_6]$ in another 400 mL of deionized water. To initiate rapid nucleation, solutions A and B were co-pumped into a rotating liquid film reactor at a controlled feed rate of 24 rpm using peristaltic pumps, with the reactor operating at ~1500 rpm for 10 minutes. The resulting slurry was subsequently transferred to a four-necked flask and subjected to aging at 80 °C for 10 hours under a nitrogen atmosphere, accompanied by continuous magnetic stirring (600 rpm). Post-aging, the precipitate was isolated *via* repeated centrifugation and thoroughly washed with deionized water until the supernatant reached a neutral pH (≈7). Finally, the purified solid product was divided into four equal portions for subsequent characterization and application studies.

Synthesis of Mn-PB@LDHs. To engineer Mn-doped Prussian blue intercalated within MgAl-LDHs (denoted as Mn-PB@LDHs) with controlled Mn^{2+}/Fe^{2+} molar ratios, a series of composite materials *via* a sequential doping strategy using methanol/water mixed solvents were prepared. Specifically, PF-LDHs were first uniformly dispersed in 180 mL of a methanol/deionized water mixture (v/v = 1 : 1) to prepare solution A, which was then transferred to a four-necked flask. Separately, solution B was formulated by dissolving $MnCl_2$ and $FeCl_2$ in 10 mL of methanol at varying molar ratios (0 : 1, 1 : 9, 2 : 8, and 1 : 1) to modulate the Mn^{2+} doping level. The pH of solution A was adjusted to 4 (aqueous) using dilute HNO_3, after which

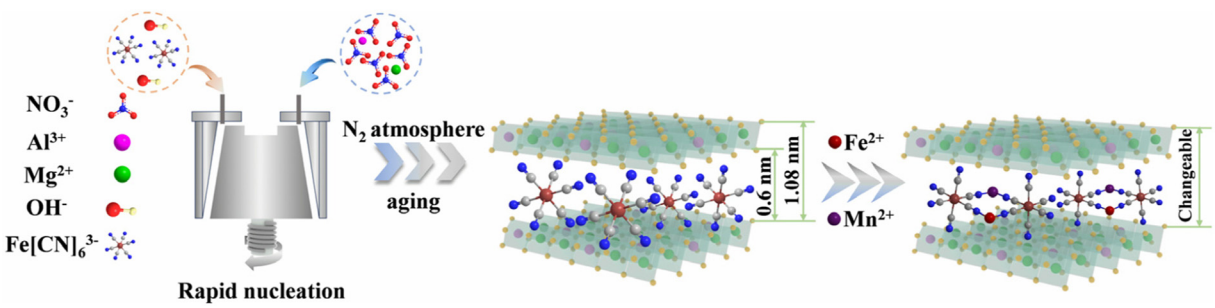

Scheme 1 Schematic illustration showing the preparation of PB@LDHs with various Mn doping.

solution B was slowly added dropwise under continuous magnetic stirring (500 rpm) at room temperature. The resulting suspension was maintained under stirring for 4 hours to ensure complete reaction and uniform Mn-PB growth on the LDH layers. Following this, the solid products were isolated *via* centrifugation, thoroughly washed with methanol to remove residual reactants, and finally freeze-dried to yield composites of the Mn-PB@LDHs, labeled Mn-PB@LDHs-1 to Mn-PB@LDHs-4 according to their respective Mn^{2+}/Fe^{2+} molar ratios.

Characterization

Structure and morphology. The crystalline structures and phase compositions of the samples of the Mn-PB@LDHs were examined by powder X-ray diffraction (XRD) on a Philips X'Pert Pro diffractometer using Cu Kα radiation (λ = 0.154056 nm) in reflection mode. Scans were performed over the 2θ range of 3–70° at a rate of 10° min^{-1}. Fourier transform infrared (FT-IR) spectra were acquired on a Thermo Nicolet 5700 spectrometer in transmission mode with a resolution of 2 cm^{-1}, using KBr pellets, across the wavenumber range of 4000–350 cm^{-1} at room temperature. Morphological and microstructural analyses were carried out using scanning electron microscopy (SEM, ZEISS Supra 55) and transmission electron microscopy (TEM, FEI Talos 200X). Optical properties were evaluated with a Shimadzu UV-3600 spectrophotometer equipped with an integrating sphere; absorption spectra were collected from 200 to 2500 nm, and diffuse reflectance spectra from 200 to 1200 nm. Raman spectra were recorded on a LabRAM Aramis spectrometer. Thermogravimetric (TG) and derivative thermogravimetric (DTG) analyses were performed on a HITACHI STA7300 instrument. Electrochemical properties, including cyclic voltammetry (CV) and electrochemical impedance spectroscopy (EIS), were measured using a CHI660E electrochemical workstation. The elemental concentrations of Mn and Fe were quantified by inductively coupled plasma optical emission spectrometry (ICP-OES, Agilent 5800).

Photothermal performance measurements. The photothermal heating profiles of Mn-PB@LDHs with varying Mn ratios were evaluated under 808 nm laser irradiation. Specifically, 0.005 g of powdered PB@LDHs or Mn-PB@LDHs was deposited on a quartz glass substrate and irradiated with an 808 nm NIR laser at a power density of 0.5 W cm^{-2} for 4 minutes. After turning off the laser, the samples were allowed to cool naturally. Temperature changes were monitored in real time using an FLIR thermal imaging camera. The photothermal conversion efficiency is calculated according to eqn (1):[4]

$$\eta = \frac{hS(T_{max} - T_{amb})}{I(1 - 10^{-A_{808}})} \quad (1)$$

where h is the heat transfer coefficient, S represents the surface area of the container, T_{max} is the maximum temperature, T_{amb} represents the ambient temperature, I is the laser power density, and A_{808} represents the absorbance of the samples at the wavelength of 808 nm.

At the maximum system temperature, the input heat equals the output heat, and the product hS can be expressed as:

$$hS = \frac{\sum_i m_i C_{p,i}}{\tau_s} \quad (2)$$

where m_i (0.43 g) and $C_{p,i}$ (0.8 J (g °C)$^{-1}$) are the mass and heat capacity of system components (including the sample and substrate), respectively, and τ_s is the system time constant. The value of τ_s was determined during the cooling phase by linear regression based on the following relation:

$$t = -\tau_s \ln \theta = -\tau_s \ln \frac{T - T_{amb}}{T_{max} - T_{amb}} \quad (3)$$

Dissolution loss experiments. The release behavior of Fe from Prussian blue and Mn-PB@LDHs-3 was systematically investigated using a previously reported method,[28] with modifications. Typically, 0.020 g of commercial Prussian blue (Macklin, Shanghai, China) or 0.071 g of Mn-PB@LDHs-3 (equivalent to 0.020 g of PB) was dispersed in 50 mL of deionized water. The suspensions were stirred magnetically for 60 min and then allowed to stand undisturbed for 30 min. Dissolution tests were also carried out under varying temperatures and alkaline conditions to evaluate their influence on Fe release. The concentration of Fe in the supernatant was determined by inductively coupled plasma atomic emission spectrometry (ICP-AES, Agilent 5800).

Solar water evaporation performance measurement. To evaluate the performance of Mn-PB@LDHs in solar-driven water evaporation, simulated solar irradiation was provided by a solar simulator (AT1 Pro, Ledesk) at an intensity of 1 kW m^{-2}. The evaporation device was constructed as follows: an air-laid paper wick was immersed in water to facilitate the continuous supply of water, while expanded polyethylene (EPE) foam was employed both for thermal insulation and mechanical support. A polytetrafluoroethylene (PTFE) filter membrane served as the water diffusion layer. Mn-PB@LDHs powder was uniformly deposited onto the PTFE membrane *via* vacuum filtration to form the photothermal evaporation layer (Scheme 2).[29] The entire device was placed on an electronic analytical balance to record the mass loss at 5-minute intervals. All experiments were conducted under ambient conditions maintained at 28.8 ± 0.3 °C and a relative humidity of 35 ± 5%.

Results and discussion

Structure and light absorption property of PB@LDHs

Fig. 1a presents the powder X-ray diffraction (XRD) patterns of Mn-PB@LDHs with varying Mn/Fe molar ratios, aiming to systematically investigate the influence of Mn^{2+} doping on their crystalline structure and interlayer organization. All samples exhibit a series of well-resolved (00l) diffraction peaks, a signature of the LDH crystallographic structure.[30] Notably, the (003) reflection corresponds to the basal spacing along the c-axis. It

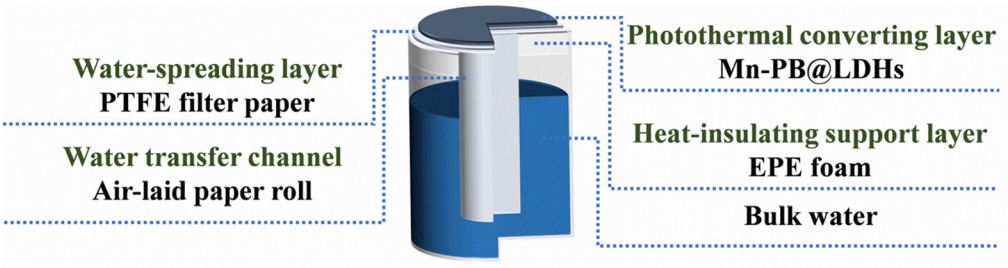

Scheme 2 A schematic diagram of the water evaporation device.

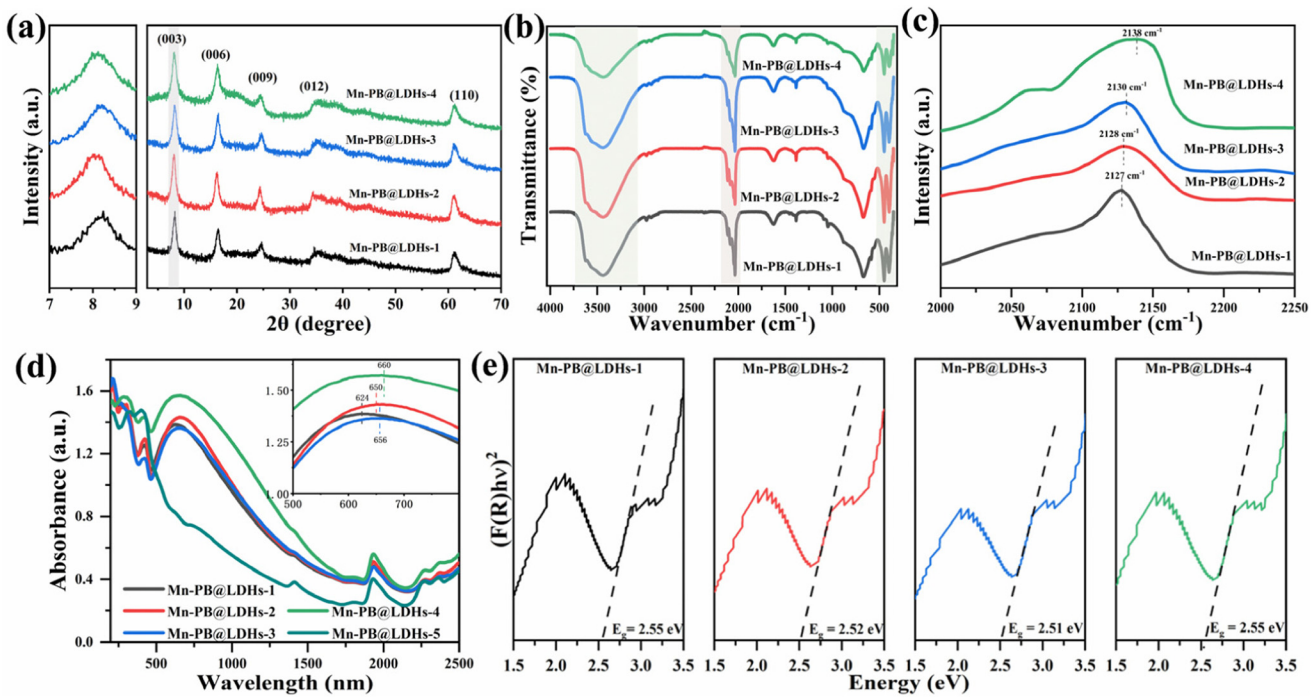

Fig. 1 (a) Powder X-ray diffraction patterns, (b) FT-IR spectra, (c) Raman spectra, and (d) UV-vis-NIR spectra of the series of Mn-PB@LDHs. (e) Band gap values of the Mn-PB@LDHs.

displays a distance of 1.08 nm and a consistent interlayer distance of 0.60 nm, confirming the successful intercalation of $[Fe(CN)_6]^{3-}$ anions within the LDH interlayer galleries (Fig. S1).[31] The appropriately sized interlayer spacing effectively stabilizes the intercalated anions through synergistic van der Waals and electrostatic interactions, thereby hindering the leaching or migration of Prussian blue (PB) species. When compared to undoped PF-LDHs, the samples of the PB@LDHs show broader and less intense diffraction peaks, indicative of reduced crystallinity and enhanced structural disorder. This phenomenon is attributed to the incorporation of divalent Mn^{2+} ions and the concurrent formation of Prussian blue-analogous nanocrystalline domains within the LDH interlayers, which disrupt the long-range atomic ordering.[32] Of particular significance, the (003) peak gradually shifts to lower diffraction angles with increasing Mn^{2+} doping, reflecting an expansion of the interlayer spacing. This shift aligns with the larger ionic radius of high-spin Mn^{2+} (0.83 Å) relative to Fe^{2+} (0.78 Å), directly correlating the structural modification to the dopant size effect.

Fig. 1b presents the Fourier-transform infrared (FT-IR) spectra of Mn-PB@LDHs with varying Mn^{2+} doping levels, aiming to characterize the chemical bonding environment and structural integrity of the composite materials. A prominent absorption band at 453 cm^{-1} is observed, which is attributed to the stretching vibrations of Mg–O and Al–O bonds in the brucite-like LDH layers, consistent with the characteristic framework vibrations of layered double hydroxides.[33,34] A broad and intense peak centered at ~3400 cm^{-1} corresponds to the O–H stretching vibrations, arising from both the hydroxyl groups in the LDH layers and the intercalated water molecules within the interlayer galleries.[35,36] Notably, two sharp peaks at 2034 and 2112 cm^{-1} are assigned to the asymmetric C≡N stretching vibrations of hexacyanoferrate(II)

($[Fe^{2+}(CN)_6]^{4-}$) and hexacyanoferrate(III) ($[Fe^{3+}(CN)_6]^{3-}$), respectively, indicating the coexistence of Fe(II) and Fe(III) oxidation states—a result of partial reduction of Fe(III) during the intercalation process of $[Fe(CN)_6]^{3-}$ into the LDH interlayers.[37,38] Additionally, a distinct peak at 586 cm^{-1} is ascribed to the Fe–C stretching vibration of the cyanide bridges, confirming the formation of well-defined Fe–CN–Fe linkages within the composite structure.[39]

Raman spectroscopy was employed to characterize the structural evolution and Mn^{2+} doping-induced modifications in PB@LDHs and Mn-PB@LDHs. In Fig. 1c, the pristine PB@LDHs exhibit a distinct Raman band at 2127 cm^{-1}, which is unambiguously assigned to the symmetric C≡N stretching vibration within the Fe–CN–Fe bridging framework of the Prussian blue analog (PBA).[40] With the progressive incorporation of Mn^{2+} ions into the PBA lattice, this characteristic peak undergoes a systematic blue-shift, shifting to 2128 cm^{-1} (Mn-PB@LDHs-2), 2130 cm^{-1} (Mn-PB@LDHs-3), and 2138 cm^{-1} (Mn-PB@LDHs-4). This wavenumber upshift provides direct evidence of local lattice distortion and altered bonding interactions between cyanide ligands and metal centers, primarily attributed to the insertion of Mn^{2+} ions into the PBA framework. The presence of Mn^{2+} likely induces the formation of cyanide vacancies or localized structural defects adjacent to the dopant sites,[41] thereby reshaping the vibrational microenvironment of the CN^- bridges. These structural modifications are hypothesized to critically influence key material properties, including electronic conductivity, charge transfer kinetics, and ultimately photothermal conversion efficiency, by altering the electronic structure and interfacial interactions within the composite.

The optical absorption properties of the PB@LDHs and Mn-PB@LDHs were systematically investigated using UV-vis-NIR spectroscopy to elucidate the effect of Mn^{2+} incorporation on light-harvesting capabilities. In Fig. 1d, pristine PB@LDHs exhibit a broad visible-near-infrared (vis-NIR) absorption band spanning 500–1000 nm, with a distinct absorption maximum centered at 624 nm. This characteristic peak is attributed to intervalence metal-to-metal charge transfer (MMCT) transitions between Fe^{2+} and Fe^{3+} ions mediated by cyanide bridges in the Prussian blue analog (PBA) framework.[42] Upon progressive Mn^{2+} doping, the absorption maximum undergoes a systematic red-shift, shifting to 650 nm (Mn-PB@LDHs-2), 656 nm (Mn-PB@LDHs-3), and 660 nm (Mn-PB@LDHs-4). This red-shift phenomenon arises from alterations to the local electronic structure induced by Mn^{2+} substitution: the incorporation of Mn^{2+} ions modifies the electron density distribution and orbital energy levels within the Fe–CN–Fe coordination motif, while reducing the symmetry of the MMCT pathway and introducing lattice strain. These combined effects collectively reshape the energy landscape of the Fe–CN bonding system, thereby shifting the MMCT transition energy to lower wavenumbers.[42,43]

To elucidate the specific role of Mn^{2+} in modulating the optical properties of PB@LDHs, a control sample (Mn-PB@LDHs-5) was synthesized using a $MnCl_2$: $FeCl_2$ precursor ratio of 1 : 0 (Fig. S2), designed to isolate the contribution of Mn^{2+} to light absorption. As shown in Fig. 1d, the absorption profile of Mn-PB@LDHs-5 reveals only a weak vis-NIR band spanning 500–1000 nm, indicating negligible intrinsic light-harvesting capability of Mn-PB alone. This result confirms that the enhanced absorption in Mn-PB@LDHs originates predominantly from the Fe-mediated metal-to-metal charge transfer (MMCT) transitions, with Mn^{2+} functioning not as a primary light absorber but as an electronic modulator that perturbs the Fe–CN bonding network. These findings underscore the critical role of Mn incorporation in fine-tuning the electronic structure and optical behavior of PB@LDHs, which is expected to exert a significant influence on their photothermal conversion efficiency.

The band gap energies of the Mn-PB@LDHs samples were evaluated using the Kubelka–Munk (K–M) transformation:[44,45]

$$F(R_\infty)h\nu = C(h\nu - E_g)^q \quad (4)$$

where $F(R_\infty)$ is the K–M function, R_∞ is the reflectance, h is Planck's constant (4.135×10^{-15} eV s), ν is photon frequency (s^{-1}), E_g is the band gap energy, C is a proportionality constant, and q is an exponent that depends on the nature of the electronic transition, being equal to 1/2 for a direct transition and 2 for an indirect transition.

Fig. 1e presents the band gap values for Mn–Prussian blue intercalated layered double hydroxides (Mn-PB@LDHs) with varying Mn^{2+} doping levels (Mn-PB@LDHs-1 to Mn-PB@LDHs-4), aiming to quantify the effect of Mn incorporation on the electronic band structure. The computed band gaps are 2.55 eV (Mn-PB@LDHs-1), 2.52 eV (Mn-PB@LDHs-2), 2.51 eV (Mn-PB@LDHs-3), and 2.55 eV (Mn-PB@LDHs-4), collectively indicating that Mn^{2+} doping exerts a subtle yet discernible regulatory effect on the electronic band structure of the host PB@LDHs. This minor variability in band gap energy arises from Mn^{2+}-induced electron density redistribution and alterations to the local coordination environment of the Fe–CN–Fe bridging motifs, which collectively modify the energy levels of the valence and conduction bands. Additionally, the Jahn–Teller effect—characteristic of high-spin Mn^{2+} (d^5 configuration)—may induce localized structural distortions in the octahedral coordination geometry, further contributing to the observed fluctuations in the optical band gap. This experimental–theoretical correlation underscores the utility of Mn doping as a precise strategy for tailoring the electronic properties of PB@LDHs, providing critical insights for optimizing their light–matter interaction and photothermal performance.

Fig. 2 systematically characterizes the morphological features of Mn-PB@LDHs with varying Mn^{2+} doping levels, highlighting their structural integrity and compositional homogeneity at the microscale. All samples exhibit well-defined lamellar stacking architectures, retaining the intrinsic layered morphology hallmark of LDH materials synthesized *via* the separate nucleation and aging steps (SNAS) method.[46] This structure confirms the preservation of the layered framework during Mn-PB intercalation. Elemental mapping analyses *via* energy-

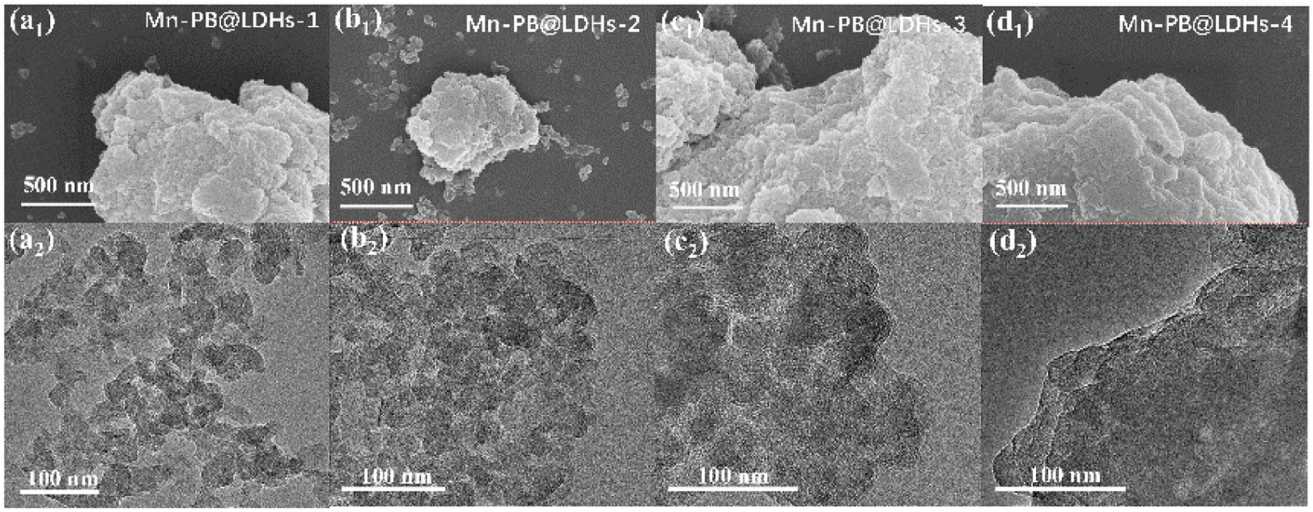

Fig. 2 Morphologies of different Mn doping amounts of Mn-PB@LDHs: (a) Mn-PB@LDHs-1, (b) Mn-PB@LDHs-2, (c) Mn-PB@LDHs-3 and (d) Mn-PB@LDHs-4; (a_1–d_1) SEM images and (a_2–d_2) TEM images.

dispersive X-ray spectroscopy (EDS) (Fig. 3) reveal the uniform and homogeneous distribution of both Fe and Mn throughout the LDH platelets. This uniform dispersion strongly indicates the successful intercalation of Mn-doped Prussian blue analogues within the LDH interlayer galleries, avoiding significant surface agglomeration or phase segregation. The effective integration of Mn-modified PB species into the LDH host matrix is anticipated to enhance the structural integrity and promote synergistic interplay between Mn-PB and LDHs, thereby creating a favorable microenvironment for improved photothermal conversion efficiency.

Structure stability analysis

Thermogravimetric analysis (TGA) and differential thermogravimetry (DTG) were systematically employed to elucidate the thermal decomposition kinetics and compositional evolution of Mn-PB@LDHs and pristine Prussian blue (PB) (Fig. 4 and Fig. S3). All Mn-PB@LDHs samples exhibited a characteristic three-stage weight loss profile upon controlled heating, with distinct derivative thermogravimetric (DTG) peaks corresponding to each decomposition step. The first minor mass loss (<200 °C) was attributed to the desorption of physisorbed water and interlayer water molecules.[47] The second stage, spanning 200–310 °C, involved intensive dehydroxylation of the brucite-like MgAl-LDH layers, manifesting as a prominent DTG peak in this temperature range. The final and most significant weight loss (>310 °C) comprised two concurrent processes: further dehydroxylation of the LDH host framework and the thermal decomposition of intercalated Prussian blue (PB) analog molecules into iron oxide species.

For comparative insight, pristine PB was also analyzed *via* TGA (Fig. S3), displaying a three-step decomposition pathway with distinct thermal thresholds: an initial mild mass loss (<180 °C) due to surface water desorption; a subsequent exothermic event (180–260 °C) associated with the release of cyanide ligands ($[Fe(CN)_6]^{4-}$); and a final high-temperature step (>260 °C) leading to the formation of iron oxide (*e.g.*, Fe_2O_3) as the stable decomposition product.[48] Notably, the PB decomposition exhibited a sharper exothermic DTG peak compared to Mn-PB@LDHs, reflecting more rapid and synchronized thermal decomposition kinetics during ligand release and oxide formation.[49] Interestingly, an unexpected temperature drop was observed during the decomposition of PB. This can be attributed to two factors. First, the decomposition releases a significant volume of gases, whose rapid escape carries away sensible heat. Second, the decomposition process also involves endothermic processes that further reduce the system temperature.

Notably, Mn-PB@LDHs exhibit superior thermal stability compared to pristine Prussian blue (PB), a critical advancement attributed to synergistic stabilizing mechanisms inherent to their composite architecture. This enhanced thermal performance stems from two primary factors: first, the van der Waals confinement imposed by the LDH interlayers restricts the structural mobility of PB, effectively delaying their thermal collapse; second, electrostatic interactions between the anionic cyanide ($[Fe(CN)_6]^{4-}$) groups of PB and the positively charged MgAl-LDH host layers inhibit the dissociation of cyanide ligands. These combined effects fundamentally alter the degradation pathway of PB, decoupling its breakdown from the conventional cyanide release-dominated process[50] and thereby stabilizing the material against thermal decomposition.

To assess the aqueous stability of the optimal Mn-PB@LDHs-3, its metal leaching behavior was systematically compared with that of conventional insoluble Prussian blue (PB).[51] Quantitative analysis of Fe leaching concentrations (Fig. 4c) revealed that the dissolution rate of Mn-PB@LDHs-3 was nearly 50% lower than that of pristine insoluble PB and significantly reduced compared to soluble PB, which typically

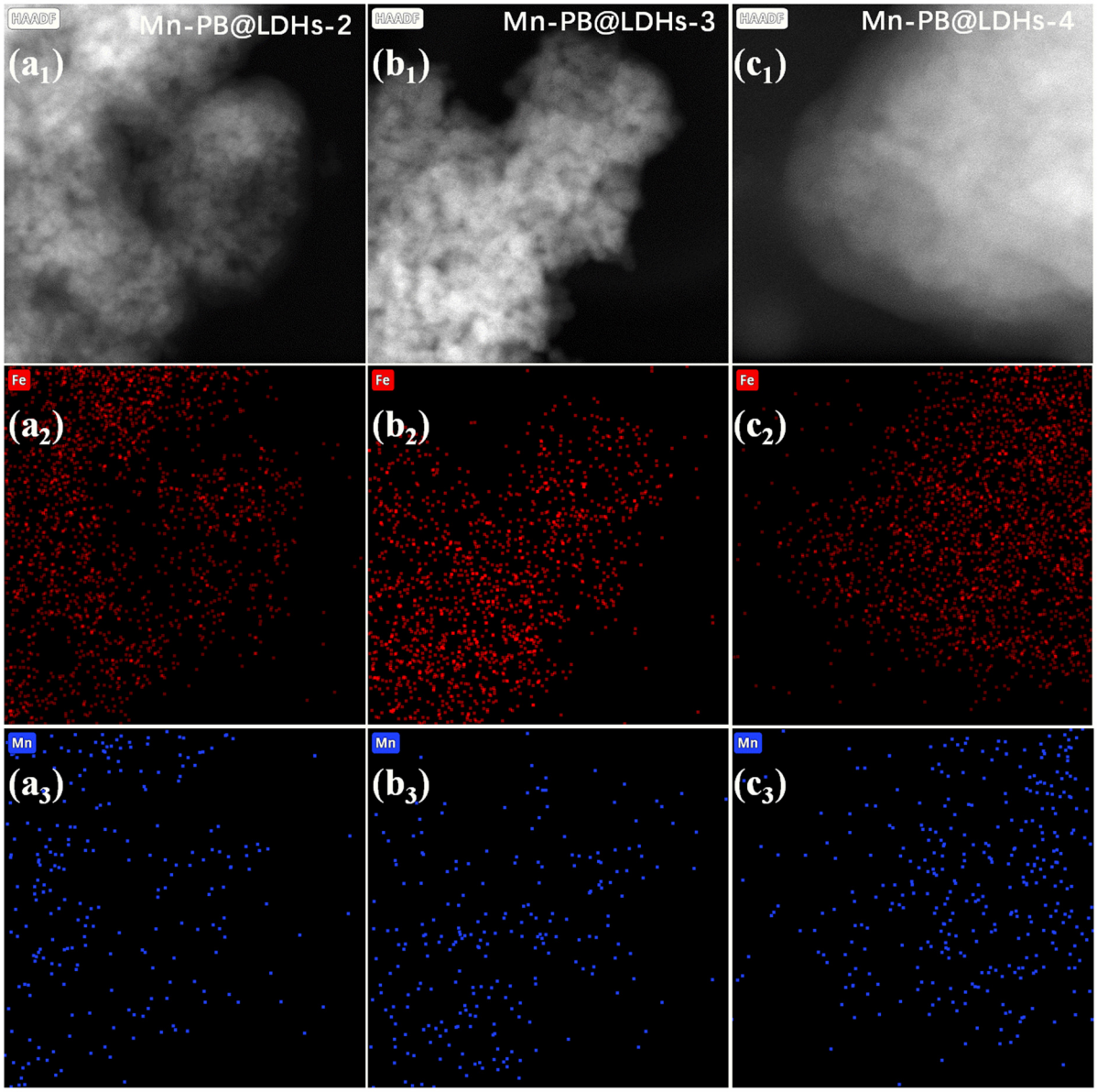

Fig. 3 (a_1–c_1) TEM images and (a_2–c_3) EDS elemental mapping of Mn-PB@LDHs: (a) Mn-PB@LDHs-1, (b) Mn-PB@LDHs-2, (c) Mn-PB@LDHs-3, and (d) Mn-PB@LDHs-4.

exhibit pronounced dissociation in aqueous environments.[28] Notably, Mn-PB@LDHs-3 displayed temperature-independent dissolution behavior across all tested conditions, confirming the critical stabilizing role of LDH nanoconfinement in mitigating PB degradation under aqueous conditions.

To further evaluate the chemical stability of Mn-PB@LDHs-3 under alkaline conditions, its Fe dissolution behavior was systematically investigated in $NaHCO_3$–Na_2CO_3 buffer solutions (pH = 10). The solution was prepared as follows: first, 0.21 g of sodium bicarbonate was dissolved in 120 mL of deionized water. Subsequently, 0.1 mol L^{-1} sodium hydroxide solution was added dropwise to this solution under continuous stirring until the pH stabilized at 10. While pristine Prussian blue (PB) underwent rapid decomposition under these alkaline environments, forming reddish-brown $Fe(OH)_3$ precipitates *via* ligand displacement reactions, Mn-PB@LDHs-3 maintained its structural integrity with no visible reddish-brown precipitation observed (Fig. 4d). Quantitative analysis *via* inductively coupled plasma atomic emission spectrometry (ICP-AES) revealed a dissolved Fe concentration of 25.92 mg L^{-1}, demonstrating exceptional alkaline stability. This enhanced robustness stems from two synergistic stabilization mechanisms: (i) spatial confinement of PB within the LDH interlayer galleries, which physically restricts ligand exchange; and (ii) electrostatic anion shielding by the positively charged MgAl-LDH host layers, which effectively inhibits the release of

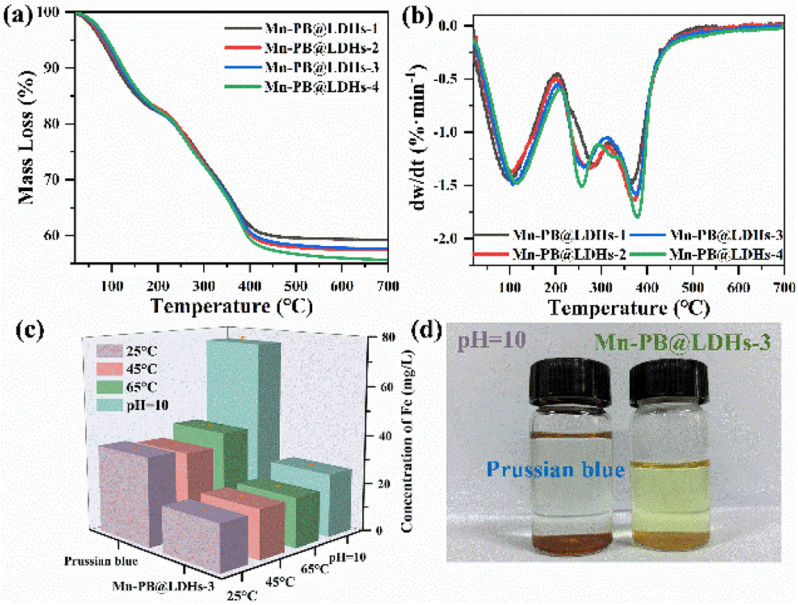

Fig. 4 (a) TG curves and (b) DTG curves of Mn-PB@LDHs under an air atmosphere and heating rate of 10 °C min^{-1}. (c) Concentration of Fe dissolved from Prussian blue/Mn-PB@LDHs-3. (d) Digital image of Prussian blue (left) and Mn-PB@LDHs-3 (right) after exposure to an alkaline environment (pH = 10) for 60 minutes.

PB species. Collectively, this dual stabilization strategy not only enhances the environmental compatibility of Prussian blue-based materials but also establishes a generalizable design principle for developing hydrolysis-resistant coordination polymers through host–guest nanoconfinement engineering.

Photothermal conversion property analysis

Table 1 summarizes the experimentally quantified Mn doping concentrations in Mn-PB@LDHs, revealing critical insights into the doping behavior and its dependency on precursor feed ratios. The data demonstrate a positive correlation between Mn doping levels and the increasing $MnCl_2$ precursor ratio, where higher feed ratios initially lead to proportional enhancements in Mn incorporation. Notably, however, a saturation effect emerges beyond a critical doping threshold of 2.46‰: further increasing the Mn precursor feed ratio by over 2.5-fold results in only a negligible rise in the actual Mn content integrated into the composites. This plateau in doping efficiency is attributed to interfacial interactions between the PB guest and LDH host: the strong electrostatic attraction between anionic cyanide ligands ($[Fe(CN)_6]^{4-}$) in PB and the positively charged MgAl-LDH layers creates a steric and electronic barrier that impedes additional Mn^{2+} coordination, thereby limiting further doping and preserving the structural integrity of the Mn-PB@LDH hybrids.

Table 1 Concentration of Mn doped into PB@LDHs

	Concentration of Mn (mg L^{-1})	Ratio of Mn in LDHs (‰)	Ratio of Mn in PB (‰)
Mn-PB@LDHs-1	—	—	—
Mn-PB@LDHs-2	0.16	0.62	2.21
Mn-PB@LDHs-3	0.63	2.46	8.76
Mn-PB@LDHs-4	0.77	2.82	10.05

The photothermal conversion performance of Mn-PB@LDHs under 808 nm near-infrared (NIR) laser irradiation was systematically evaluated to elucidate the influence of Mn^{2+} doping on light-to-heat conversion efficiency (Fig. 5a). As shown in Fig. 5b, Mn-PB@LDHs-1, Mn-PB@LDHs-2, and Mn-PB@LDHs-3 (with increasing Mn doping levels) displayed a monotonic temperature rise over 4 minutes of continuous 808 nm NIR laser irradiation (0.5 W cm^{-2}), reaching maximum surface temperatures of 87.4 °C, 91.4 °C, and 99.0 °C, respectively. This trend confirms that moderate Mn doping significantly enhances the photothermal response of the PB@LDH composites. However, further increasing the Mn doping ratio (beyond the optimal threshold) led to a diminished heating effect, with the maximum temperature plateauing at only 88.3 °C. This non-monotonic behavior indicates that excessive Mn^{2+} integration disrupts the intra-Prussian blue electron transport dynamics, impairing the efficient conversion of absorbed light energy into heat. In contrast, the LDH host layers contributed minimally to NIR light absorption due to their inherently weak optical activity in this spectral range, suggesting that the photothermal enhancement primarily originates from the Mn-modified PB moieties.

To further elucidate the photothermal behavior of the optimal Mn-PB@LDH hybrid (Mn-PB@LDHs-3), its temperature evolution under varying near-infrared (NIR) laser power densities was systematically investigated to quantify the

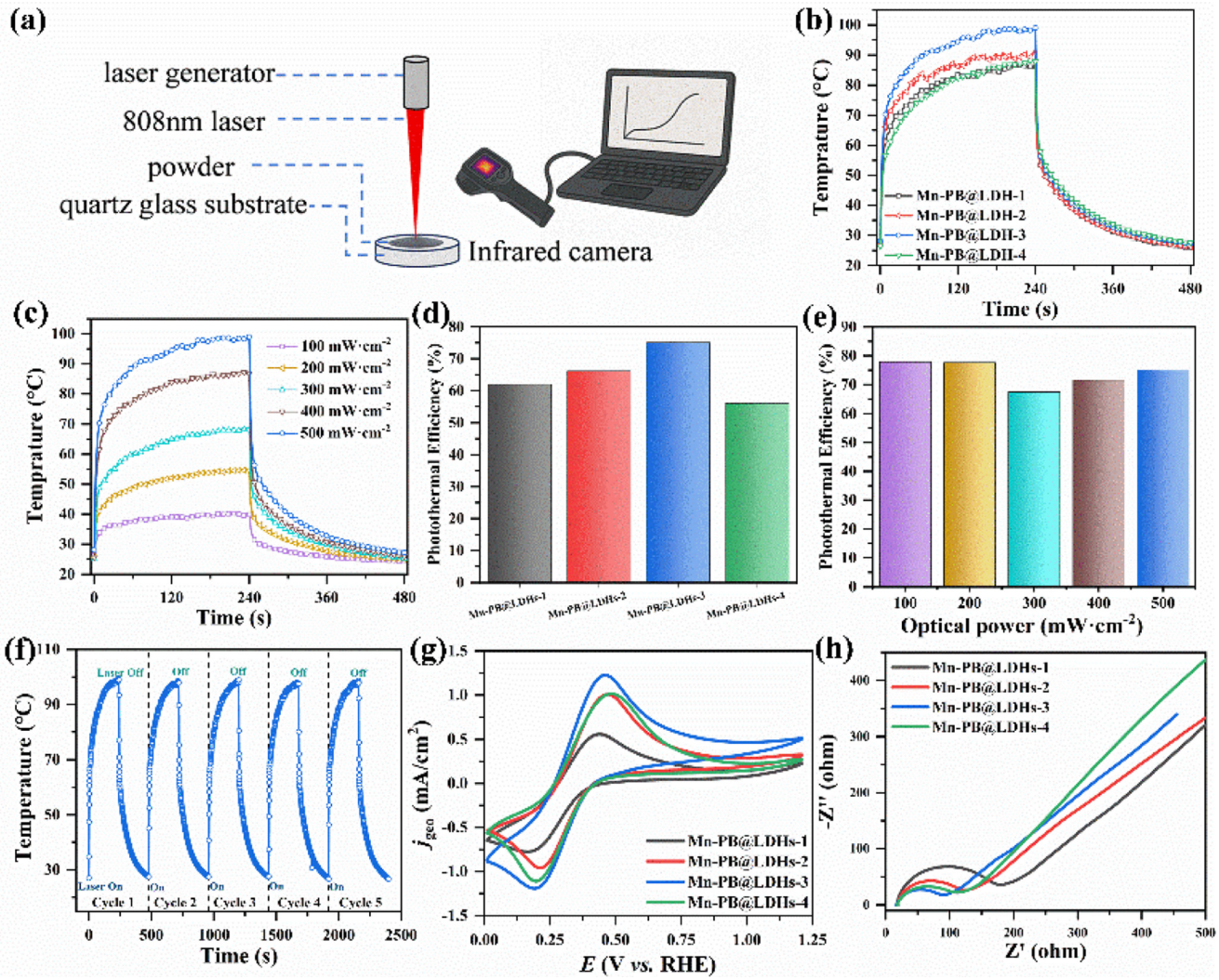

Fig. 5 The photothermal conversion properties and electron transport performances of variously Mn-doped PB@LDHs. (a) Schematic diagram of the photothermal conversion setup. (b) The temporal temperature variation of variously Mn-doped powders of PB@LDHs. (c) The temporal–temperature variation of Mn-PB@LDHs-3 at different power densities. (d) The photothermal conversion efficiency of variously Mn-doped powders of PB@LDHs. (e) The photothermal conversion efficiency of Mn-PB@LDHs-3 at different power densities. (f) Photothermal profiles of Mn-PB@LDHs-3 over five cycles under 808 nm irradiation (0.5 W cm^{-2}). (g) CV curves and (h) EIS curves of variously Mn-doped PB@LDHs.

relationship between light intensity and photothermal conversion efficiency. As illustrated in Fig. 5c, the equilibrium surface temperature of Mn-PB@LDHs-3 increased monotonically with rising laser power density, reaching 40.4 °C, 55.1 °C, 68.8 °C, 87.2 °C, and 99.0 °C under irradiation intensities of 0.1, 0.2, 0.3, 0.4, and 0.5 W cm^{-2}, respectively. This linear dependence of temperature on laser power density conclusively demonstrates the efficient and controllable photothermal conversion behavior of the Mn-PB@LDH composites. Notably, this observation underscores that optimal Mn doping enhances photothermal efficiency by optimizing the electronic configuration of the Prussian blue framework—facilitating more effective light absorption and electron–phonon coupling—while the LDH host matrix provides critical structural integrity without undermining the NIR photothermal activity.

To comprehensively evaluate the photothermal conversion efficiency (η) of Mn-PB@LDHs and elucidate the influence of Mn^{2+} doping on light-to-heat performance, we conducted quantitative analyses using characteristic time constants (τ_s) and steady-state temperature measurements. As shown in Fig. 5d and Fig. S4, moderate Mn incorporation significantly enhances η: values increase from 61.97% for pristine PB@LDHs to 66.15% for Mn-PB@LDHs-2, peaking at 75.10% for Mn-PB@LDHs-3. This non-monotonic trend—where excessive Mn doping (Mn-PB@LDHs-4) reduces efficiency—confirms the existence of an optimal doping concentration that maximizes photothermal conversion. Further characterization reveals the robustness of Mn-PB@LDHs-3: its η remains nearly unchanged across varying laser power densities (0.1–0.5 W cm^{-2}, Fig. 5e and Fig. S5), demonstrating consistent performance under diverse irradiation intensities. To assess oper-

ational stability, cyclic photothermal tests were performed *via* repeated laser on/off cycles (808 nm, 0.5 W cm^{-2}, 4 min irradiation + 4 min cooling). As illustrated in Fig. 5f, the sample exhibits no significant degradation in heating/cooling profiles over five consecutive cycles, confirming excellent photothermal reversibility and long-term durability under practical conditions.

To decipher the mechanistic origin of the enhanced photothermal conversion efficiency (η) in Mn-PB@LDHs, we conducted electrochemical characterizations—including cyclic voltammetry (CV) and electrochemical impedance spectroscopy (EIS)—on samples with graded Mn doping levels. As illustrated in Fig. 5g and h, the charge transfer resistance (R_{ct}) exhibits a non-monotonic dependence on Mn content: it first decreases to a minimum at moderate doping (Mn-PB@LDHs-3) and then increases with excessive Mn incorporation. This trend identifies Mn-PB@LDHs-3 as the optimal variant for efficient charge transport within the series. Mechanistically, Mn^{2+} ions initially occupy cyanide (CN^-) vacancies in the PB@LDHs lattice, creating additional pathways for electron delocalization along the CN^- bridging networks and thus reducing R_{ct}. However, beyond the optimal doping threshold, excess Mn^{2+} preferentially substitutes Fe^{2+} sites in the brucite-like layers, disrupting the Fe^{3+}/Fe^{2+} redox couple dynamics across the CN^- coordination framework and impeding long-range electron transfer. Concurrently, high Mn^{2+} concentrations induce structural distortions *via* the Jahn–Teller effect: although Mn^{2+} ($3d^5$) typically adopts a near-regular octahedral geometry with suppressed distortion, partial oxidation of Mn^{2+} to Mn^{3+} (or higher valence states) leads to uneven population of the e_g orbital set ($d_{x^2-y^2}$ and d_{z^2}). Specifically, the remaining electron preferentially occupies the lower-energy d_{z^2} orbital, strengthening its shielding of the Mn nucleus, while the higher-energy $d_{x^2-y^2}$ orbital remains less shielded. This electronic asymmetry reduces the symmetry of the Mn–N_6 coordination polyhedron, causing localized contraction of the octahedral units. Furthermore, the contraction of Mn–N bonds within the *xy*-plane intensifies repulsion between the N 2p orbitals and Mn d_{xy} orbitals, elevating the energy of the d_{xy} orbital while stabilizing the d_{xz} and d_{yz} orbitals. This electronic reorganization destabilizes the crystal lattice, impedes charge transport by increasing interatomic resistance, and ultimately diminishes photothermal conversion efficiency at excessive Mn doping levels.[40,52]

Solar water generation property measurement

The photothermal water evaporation performance of Mn-PB@LDHs under solar irradiation was systematically investigated to elucidate the effect of Mn^{2+} doping on evaporation efficiency. As shown in Fig. 6a and b, the water evaporation rate exhibited a monotonic increase with moderate Mn doping, rising from 1.56 kg m^{-2} h^{-1} for Mn-PB@LDHs-1 to 1.59 kg m^{-2} h^{-1} for Mn-PB@LDHs-2 and reaching a peak of 1.60 kg m^{-2} h^{-1} for Mn-PB@LDHs-3. However, further increasing the Mn doping level (Mn-PB@LDHs-4) resulted in a slight performance decline, with an evaporation rate of 1.59 kg m^{-2} h^{-1}. The surface temperature evolution of the evaporation system was investigated under simulated solar irradiation (1 kW m^{-2}, Xe lamp, AM1.5G filter) for 6 min, with the temperature monitored by an infrared (IR) thermal camera (Fig. 6c).

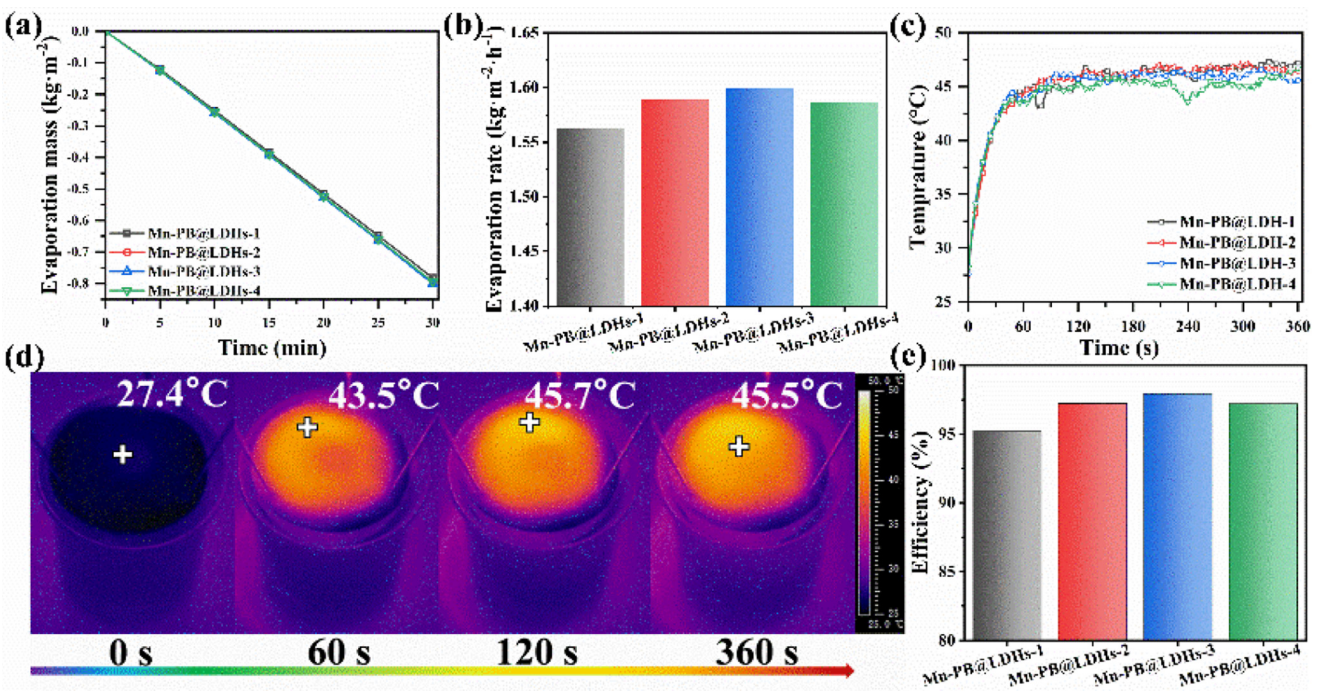

Fig. 6 (a) Mass loss curves, (b) evaporation rate comparison, (c) the time-dependent surface temperature of Mn-doped PB@LDHs, (d) IR camera images of Mn-PB@LDHs-3 under 1.0 Sun irradiation and (e) solar-to-vapor conversion efficiency of Mn-PB@LDHs.

Upon irradiation, the top surface rapidly absorbed incident photons and converted them into heat, leading to a sharp temperature increase. As shown in Fig. 6d, the temperature of Mn-PB@LDHs-3 rose steeply within 1 min and reached a stable equilibrium after approximately 2 min, reflecting its excellent photothermal conversion capability.

The solar-to-vapor conversion efficiency (η) was calculated using the following equations:[53]

$$\eta = m(H_{LV} + Q)/E_{in} \quad (5)$$

$$H_{LV}(T) = 1.91846 \times 10^6[T_1/(T_1 - 33.91)]^2 \quad (6)$$

$$Q = c(T_1 - T_0) \quad (7)$$

where m is the water evaporation rate (kg m^{-2} h^{-1}) corrected for dark evaporation (0.18 kg m^{-2} h^{-1}), H_{LV} is the latent heat of vaporization (J kg^{-1}) at equilibrium temperature T_1, Q represents the sensible heat (J kg^{-1}) required to raise water from ambient temperature T_0 to T_1, E_{in} is the incident solar energy (J m^{-2} h^{-1}), and c is the specific heat capacity of water (4.2 J g K^{-1}).

As shown in Fig. 6e, the solar-to-vapor conversion efficiency (η) values of Mn-PB@LDHs-1 to Mn-PB@LDHs-4 were determined to be 95.22%, 97.24%, 97.93%, and 97.22%, respectively. This trend closely follows the water evaporation rates. The non-monotonic variation is attributed to excessive Mn^{2+} incorporation, which perturbs the electronic structure of the Prussian blue framework, partially inhibits electron transitions, and thereby reduces photothermal conversion efficiency. Although the performance differences among the four samples are modest due to the low overall Mn doping content, a clear doping-dependent trend is observable. These results demonstrate that precise Mn doping modulation serves as an effective strategy for tailoring electron transport dynamics within PB@LDHs, enabling targeted optimization of their photothermal water evaporation performance.

Conclusions

In summary, this comprehensive study establishes that the synergistic integration of Mn^{2+} doping and layered double hydroxide (LDH) host confinement represents a powerful strategy to enhance both the photothermal conversion efficiency and environmental stability of Prussian blue (PB)-based materials. The optimally engineered Mn-PB@LDHs-3 exhibits exceptional performance metrics, including a record-high photothermal conversion efficiency of 75.10% under 808 nm laser irradiation and a solar-driven water evaporation rate of 1.60 kg m^{-2} h^{-1} and solar-to-vapor conversion efficiency of 97.93%—outperforming many reported PB-based composites. Systematic structural, spectroscopic, and electrochemical analyses reveal that moderate Mn^{2+} doping fine-tunes the electronic structure of the Fe–CN–Fe bridging framework, reducing interfacial charge transfer resistance and optimizing light-to-heat conversion kinetics. Conversely, excessive Mn incorporation induces lattice distortion and localized electronic localization, which degrade photothermal efficacy by disrupting coherent charge transport. Critically, the LDH host layers play a dual stabilizing role: their nanoconfinement geometry physically restricts PB framework degradation, while electrostatic interactions between the positively charged LDH layers and anionic cyanide ligands in PB suppress metal leaching and structural disintegration under aqueous and alkaline conditions. Although the photothermal performance of the material is still limited by the intrinsic instability of the Fe–CN structure and relatively narrow absorption bandwidth, these findings not only advance the development of high-performance photothermal materials but also open new avenues for designing next-generation solar energy conversion systems, such as solar-driven desalination and photocatalytic reactors, where durability and efficiency are equally critical.

Conflicts of interest

The authors declare that they have no known competing financial interests or personal relationships that could have appeared to influence the work reported in this paper.

Data availability

All data required to evaluate the conclusions of the dissertation appear in the paper including the supporting information (SI). Other relevant data supporting the findings of this study are available from the corresponding author Y. J. Feng (yjfeng@mail.buct.edu.cn), upon reasonable request.

Supplementary information is available, for example, XRD patterns of PF@LDHs and Mn-PB@LDHs-5, TG-DTG curves and (b) DTA curves of pure Prussian blue, The time-lnθ linear curves at 500 mW·cm-2 of (a) Mn-PB@LDHs-1, (b) Mn-PB@LDHs-2, (c) Mn-PB@LDHs-3 and (d) Mn-PB@LDHs-4, and The time-lnθ linear curves of Mn-PB@LDHs-3 at (a) 100 mW cm^{-2}, (b) 200 mW cm^{-2}, (c) 300 mW cm^{-2}, (d) 400 mW cm^{-2} and (e) 500 mW cm^{-2}. See DOI: https://doi.org/10.1039/d5dt02778k.

Acknowledgements

This work was financially supported by the Mount Tai Industrial Leading Talent Project and Science and Technology Program of XPCC' (No. 2024DA012).

References

1 B. Lü, Y. Chen, P. Li, B. Wang, K. Müllen and M. Yin, Stable radical anions generated from a porous perylenediimide metal-organic framework for boosting near-infrared photothermal conversion, *Nat. Commun.*, 2019, **10**, 767.

2 R.-L. Ge, P.-N. Yan, Y. Liu, Z.-S. Li, S.-Q. Shen and Y. Yu, Recent advances and clinical potential of near infrared photothermal conversion materials for photothermal hepatocellular carcinoma therapy, *Adv. Funct. Mater.*, 2023, **33**, 2301138.

3 D. Yan, M. Wang, Q. Wu, N. Niu, M. Li, R. Song, J. Rao, M. Kang, Z. Zhang, F. Zhou, D. Wang and B. Z. Tang, Multimodal imaging-guided photothermal immunotherapy based on a versatile NIR-II aggregation-induced emission luminogen, *Angew. Chem., Int. Ed.*, 2022, **61**, e202202614.

4 Y. Wang, W. Zhu, W. Du, X. Liu, X. Zhang, H. Dong and W. Hu, Cocrystals strategy towards materials for near-infrared photothermal conversion and imaging, *Angew. Chem., Int. Ed.*, 2018, **57**, 3963–3967.

5 S. Zhu, B. Zhao, M. Li, H. Wang, J. Zhu, Q. Li, H. Gao, Q. Feng and X. Cao, Microenvironment responsive nanocomposite hydrogel with NIR photothermal therapy, vascularization and anti-inflammation for diabetic infected wound healing, *Bioact. Mater.*, 2023, **26**, 306–320.

6 F. Zhu, Y. Gao and J. Qiu, Sr_2AlTaO_6: Ni^{2+} phosphors with excellent IQE and thermal stability as NIR-II source for night vision, nonvisual detection, and far-field imaging, *Chem. Eng. J.*, 2025, **505**, 159559.

7 Y. Yan, Z.-Y. Li, N.-N. Zhang and H. Krautscheid, A π–π stacked porous framework for highly efficient second near-infrared photothermal effects and photo-thermo-electric conversion, *Chem. Eng. J.*, 2024, **499**, 156059.

8 C. Liu, H. Zhang, Q. Wang, J. Wu, P. Chen, S. Song, C. Zhan, L. Wang and F. Jia, Efficient gold recovery from low concentrated $Au(S_2O_3)_2^{3-}$ solution through enhanced photocatalysis via photothermal and surface plasmon resonance assistance on MoS_2/MXene/Ag, *Desalination*, 2024, **584**, 117733.

9 H. Lim, M. Kim, J. Yoo, D. Lee, M. Lee, B. Na and S. K. Kim, Environmentally safe and renewable solar vapor generation device based on prussian blue nanoparticles immobilized on cellulose nanofibers, *Desalination*, 2022, **524**, 115477.

10 Y. Lu, J. Xu, C. Zhao, Z. Gao and Y.-Y. Song, Boosting the local temperature of hybrid prussian blue/NiO nanotubes by solar light: effect on energy storage, *ACS Sustainable Chem. Eng.*, 2021, **9**, 11837–11846.

11 Y. Huang, D. Ye, J. Yang, H. Lu, L. Li and Y. Ding, A novel dual-signal molecularly imprinted electrochemical sensor based on NiFe prussian blue analogue and SnS_2 for detection of p-hydroxyacetophenone, *Chem. Eng. J.*, 2022, **435**, 134981.

12 Y. Xiao, J. Xiao, H. Zhao, J. Li, G. Zhang, D. Zhang, X. Guo, H. Gao, Y. Wang, J. Chen, G. Wang and H. Liu, Prussian blue analogues for sodium-ion battery cathodes: a review of mechanistic insights, current challenges, and future pathways, *Small*, 2024, **20**, 2401957.

13 M. Zhou, X. Tian, Y. Sun, X. He, H. Li, T. Ma, Q. Zhao and J. Qiu, Pillar effect boosting the electrochemical stability of prussian blue-polypyrrole for potassium ion batteries, *Nano Res.*, 2023, **16**, 6326–6333.

14 Q. Tao, G. He, S. Ye, D. Zhang, Z. Zhang, L. Qi and R. Liu, Mn doped prussian blue nanoparticles for T1/T2 MR imaging, PA imaging and fenton reaction enhanced mild temperature photothermal therapy of tumor, *J. Nanobiotechnol.*, 2022, **20**, 18.

15 Z.-H. Li, Y. Chen, Y. Sun and X.-Z. Zhang, Platinum-doped prussian blue nanozymes for multiwavelength bioimaging guided photothermal therapy of tumor and anti-inflammation, *ACS Nano*, 2021, **15**, 5189–5200.

16 J. Li, X. Liu, L. Tan, Z. Cui, X. Yang, Y. Liang, Z. Li, S. Zhu, Y. Zheng, K. W. K. Yeung, X. Wang and S. Wu, Zinc-doped prussian blue enhances photothermal clearance of staphylococcus aureus and promotes tissue repair in infected wounds, *Nat. Commun.*, 2019, **10**, 4490.

17 W. Xu, H. Zhang, J. Ou, X. Fang, F. Wang, C. Li, W. Li, Y. Hu and A. Amirfazli, Improving durability and photothermal deicing with prussian blue in ptfe superhydrophobic coating, *Mater. Lett.*, 2024, **355**, 135579.

18 P. Shou, Z. Yu, Y. Wu, Q. Feng, B. Zhou, J. Xing, C. Liu, J. Tu, O. U. Akakuru, Z. Ye, X. Zhang, Z. Lu, L. Zhang and A. Wu, Zn^{2+} doped ultrasmall prussian blue nanotheranostic agent for breast cancer photothermal therapy under MR imaging guidance, *Adv. Healthcare Mater.*, 2020, **9**, 1900948.

19 C. Wu, J. Wang, J. Li, H. Zhang, S. Sharma, L. Titheridge, C. Tiffin, Y. Fan, L. Zhao, W. Yang, Z. Li, J. Peng, J. Wang and A. T. Marshall, Achieving high OER performance by tuning the Co/Mn content in prussian blue analogues, *ACS Appl. Mater. Interfaces*, 2024, **16**, 58703–58710.

20 T. He, Q. Li, T. Lin, J. Li, S. Bai, S. An, X. Kong and Y.-F. Song, Recent progress on highly efficient removal of heavy metals by layered double hydroxides, *Chem. Eng. J.*, 2023, **462**, 142041.

21 G. Sun, J. Zhang, X. Li, B. Hao, F. Xu and K. Liu, Self-assembled morphology-controlled hierarchical Fe_3O_4 @LDH for Cr(VI) removal, *J. Environ. Chem. Eng.*, 2023, **11**, 110129.

22 S. Xu, L. Liu, X. Jia, S. Tighe, C. Zhang, H. Ma and X. Zhou, Investigation of aging resistance of organic layered double hydroxide/antioxidant composite-modified asphalt, *ACS Sustainable Chem. Eng.*, 2023, **11**, 267–277.

23 Z.-J. Tang, L.-Y. Hao, Y.-C. Zhao, L. Tian, N. Li and Z.-Q. Liu, Bridging oxygen mediated alkaline fenton catalysis in LDHs for water purification, *Appl. Catal., B*, 2025, **363**, 124828.

24 L. Ding, Z. Shen, H. Pan, Y. Chen, Y. Hu, G. Zhao, G. Hai and X. Huang, Regulating intermediate adsorption and promoting charge transfer of CoCr-LDHs by Ce doping for enhancing electrooxidation of 5-hydroxymethylfurfural, *Small*, 2025, **21**, 2409343.

25 L. Li, I. Soyhan, E. Warszawik and P. van Rijn, Layered double hydroxides: recent progress and promising perspectives toward biomedical applications, *Adv. Sci.*, 2024, **11**, 2306035.

26 Y. Zhao, F. Li, R. Zhang, D. G. Evans and X. Duan, Preparation of layered double-hydroxide nanomaterials

with a uniform crystallite size using a new method involving separate nucleation and aging steps, *Chem. Mater.*, 2002, **14**, 4286–4291.
27 Z. Li, M. Zhao, R. Tian, Y. Shi, W. Tian, Y. Bai, M. Xu, K. Xu, D. Gao and Y. Feng, An efficient synthesis and organic-modification coupling strategy to produce highly dispersed ultrathin antioxidant intercalated layered double hydroxides for enhancing performance of polypropylene composites, *Chem. Eng. J.*, 2024, **483**, 149247.
28 S. Chen, X. Yang, Z. Wang, J. Hu, S. Han, Y. Guo and T. Deng, Prussian blue analogs-based layered double hydroxides for highly efficient Cs^+ removal from wastewater, *J. Hazard. Mater.*, 2021, **410**, 124608–124618.
29 Y.-G. Wu, C.-H. Xue, X.-J. Guo, M.-C. Huang, H.-D. Wang, C.-Q. Ma, X. Wang and Z.-Y. Shao, Highly efficient solar-driven water evaporation through a cotton fabric evaporator with wettability gradient, *Chem. Eng. J.*, 2023, **471**, 144313.
30 H. Chen, R.-T. Gao, H. Chen, Y. Yang, L. Wu and L. Wang, Ruthenium and silver synergetic regulation NiFe LDH boosting long-duration industrial seawater electrolysis, *Adv. Funct. Mater.*, 2024, **34**, 2315674.
31 M. Wilhelm, M. C. Quevedo, A. Sushkova, T. L. P. Galvão, A. Bastos, M. Ferreira and J. Tedim, Hexacyanoferrate-intercalated layered double hydroxides as nanoadditives for the detection of early-stage corrosion of steel: the revival of prussian blue, *Eur. J. Inorg. Chem.*, 2020, **2020**, 2063–2073.
32 K. Rybka, J. Matusik, A. Kuligiewicz, T. Leiviskä and G. Cempura, Surface chemistry and structure evaluation of Mg/Al and Mg/Fe LDH derived from magnesite and dolomite in comparison to LDH obtained from chemicals, *Appl. Surf. Sci.*, 2021, **538**, 147923.
33 A. Zaher, W. Kamal, D. Essam, E. M. Yousry and R. Mahmoud, Repurposing Co-Fe LDH and Co-Fe LDH/Cellulose micro-adsorbents for sustainable energy generation in direct methanol fuel cells, *J. Water Process Eng.*, 2024, **62**, 105317.
34 Z. Gao, J. Liang, J. Yao, Y. Zhao, Q. Meng, G. He and H. Chen, Synthesis of Ce-doped NiAl LDH/RGO composite as an efficient photocatalyst for photocatalytic degradation of ciprofloxacin, *J. Environ. Chem. Eng.*, 2021, **9**, 105405.
35 M. Dong, Q. Luo, J. Li, K. Shi, Z. Wu and J. Tang, Reconstruction of MgAl-layered double hydroxides to LiAl-layered double hydroxides for scalable lithium extraction from salt lake brine, *Miner. Eng.*, 2023, **202**, 108293.
36 B. Zeng, Q. Wang, L. Mo, F. Jin, J. Zhu and M. Tang, Synthesis of Mg-Al LDH and its calcined form with natural materials for efficient Cr(VI) removal, *J. Environ. Chem. Eng.*, 2022, **10**, 108605.
37 R. Amini, E. Rahimpour and A. Jouyban, An optical sensing platform based on hexacyanoferrate intercalated layered double hydroxide nanozyme for determination of chromium in water, *Anal. Chim. Acta*, 1117, **2020**, 9–17.
38 Y. Shi, H. Qiu, Z. Xu, M. Chen, H. Gao, X. Yu, J. Xu and J. Cao, Boosting performance of aqueous ammonium ion batteries via Mn-partial-substituted Cu prussian blue cathode, *ACS Sustainable Chem. Eng.*, 2025, **13**, 14162–14169.
39 J. Kim, J. Kang and W. Um, Simultaneous removal of cesium and iodate using prussian blue functionalized CoCr layered double hydroxide (PB-LDH), *J. Environ. Chem. Eng.*, 2022, **10**, 107477.
40 Y. Luo, J. Shen, Y. Yao, J. Dai, F. Ling, L. Li, Y. Jiang, X. Wu, X. Rui and Y. Yu, Inhibiting the Jahn–Teller effect of manganese hexacyanoferrate via Ni and Cu codoping for advanced sodium-ion batteries, *Adv. Mater.*, 2024, **36**, 2405458.
41 X. Yu, X. Tang, J.-Y. Dong, Y. Deng, M. Saito, Z. Gao, P. M. Pancorbo, M. Marumi, W. Peterson, H. Zhang, N. Kishimoto, A. N. Alodhayb, P. K. Dwivedi, Y. Ikuhara, Y. Kitahama, T.-H. Xiao and K. Goda, Defect-engineered coordination compound nanoparticles based on prussian blue analogues for surface-enhanced raman spectroscopy, *ACS Nano*, 2024, **18**, 30987–31001.
42 W. Zhu, K. Liu, X. Sun, X. Wang, Y. Li, L. Cheng and Z. Liu, Mn^{2+}-doped prussian blue nanocubes for bimodal imaging and photothermal therapy with enhanced performance, *ACS Appl. Mater. Interfaces*, 2015, **7**, 11575–11582.
43 X. Chen, G. Wu, J. Tang, L. Zhou and S. Wei, Ytterbium – doped prussian blue: fabrication, photothermal performance and antibacterial activity, *Inorg. Chem. Commun.*, 2020, **114**, 107821.
44 S. Landi, I. R. Segundo, E. Freitas, M. Vasilevskiy, J. Carneiro and C. J. Tavares, Use and misuse of the Kubelka-Munk function to obtain the band gap energy from diffuse reflectance measurements, *Solid State Commun.*, 2022, **341**, 114573.
45 P. R. Jubu, O. S. Obaseki, D. I. Ajayi, E. Danladi, K. M. Chahrour, A. Muhammad, S. Landi, T. Igbawua, H. F. Chahul and F. K. Yam, Considerations about the determination of optical bandgap from diffuse reflectance spectroscopy using the tauc plot, *J. Opt.*, 2024, **53**, 5054–5064.
46 S. Bai, T. Li, H. Wang, L. Tan, Y. Zhao and Y.-F. Song, Scale-up synthesis of monolayer layered double hydroxide nanosheets via separate nucleation and aging steps method for efficient CO_2 photoreduction, *Chem. Eng. J.*, 2021, **419**, 129390.
47 H. Zhang, X. Hu, Y. Liu, S. Zhang and Z. Wu, Convenient synthesis of one-dimensional a-SEP@LDH via self-assembly towards simultaneously improved fire retardance, mechanical strength and thermal resistance for epoxy resin, *Composites, Part B*, 2021, **216**, 108857.
48 D. P. Domonov, S. I. Pechenyuk and Y. P. Semushina, Thermal decomposition of prussian blue analogues in various gaseous media, *J. Therm. Anal. Calorim.*, 2021, **146**, 629–635.
49 D. Parajuli, H. Tanaka, K. Sakurai, Y. Hakuta and T. Kawamoto, Thermal decomposition behavior of prussian blue in various conditions, *Materials*, 2021, **14**, 1151–1167.

50 V. Selvaraj, S. Suresh and G. Karuppasamy, Layered double hydroxide nanocomposites: a promising platform for sustainable photocatalytic solutions—a short review, *J. Nanopart. Res.*, 2025, **27**, 39.
51 Z. Wang, B. Yu, H. Alamri, S. Yarabarla, M.-H. Kim and S. D. Huang, $KCa(H_2O)_2[FeIII(CN)_6]\cdot H_2O$ nanoparticles as an antimicrobial agent against staphylococcus aureus, *Angew. Chem., Int. Ed.*, 2018, **57**, 2214–2218.
52 Q. Chen, L. Shang, C.-G. Ma and C.-K. Duan, Angular Jahn–Teller effect and photoluminescence of the tetrahedral coordinated Mn^{2+} activators in solids–a first-principles study, *Inorg. Chem.*, 2022, **61**, 13471–13480.
53 X. Wu, T. Gao, C. Han, J. Xu, G. Owens and H. Xu, A photothermal reservoir for highly efficient solar steam generation without bulk water, *Sci. Bull.*, 2019, **64**, 1625–1633.